npj | 2D materials and applications

www.nature.com/npj2dmaterials

ARTICLE OPEN

Check for updates

Twist angle dependent interlayer transfer of valley polarization from excitons to free charge carriers in $WSe_2/MoSe_2$ heterobilayers

Frank Volmer[1,2]✉, Manfred Ersfeld[1], Paulo E. Faria Junior[3], Lutz Waldecker[1,4], Bharti Parashar[5], Lars Rathmann[1], Sudipta Dubey[1], Iulia Cojocariu[5], Vitaliy Feyer[5,6], Kenji Watanabe[7], Takashi Taniguchi[8], Claus M. Schneider[5,6], Lukasz Plucinski[5], Christoph Stampfer[1,9], Jaroslav Fabian[3] and Bernd Beschoten[1,10]

Transition metal dichalcogenides (TMDs) have attracted much attention in the fields of valley- and spintronics due to their property of forming valley-polarized excitons when illuminated by circularly polarized light. In TMD-heterostructures it was shown that these electron-hole pairs can scatter into valley-polarized interlayer exciton states, which exhibit long lifetimes and a twist-angle dependence. However, the question how to create a valley polarization of free charge carriers in these heterostructures after a valley selective optical excitation is unexplored, despite its relevance for opto-electronic devices. Here, we identify an interlayer transfer mechanism in twisted $WSe_2/MoSe_2$ heterobilayers that transfers the valley polarization from excitons in WSe_2 to free charge carriers in $MoSe_2$ with valley lifetimes of up to 12 ns. This mechanism is most efficient at large twist angles, whereas the valley lifetimes of free charge carriers are surprisingly short for small twist angles, despite the occurrence of interlayer excitons.

npj 2D Materials and Applications (2023)7:58 ; https://doi.org/10.1038/s41699-023-00420-1

INTRODUCTION

Using excitons in transition metal dichalcogenides (TMDs) to store and manipulate information in their valley degree of freedom is argued to be an appealing alternative to charge-based information processing[1–5]. Especially heterostructures made from two different, semiconducting TMDs, like $WSe_2/MoSe_2$-heterobilayers, are of great interest as excitons in these heterobilayers can be controlled by electrical means[6–9] and exhibit recombination and valley lifetimes in the nanosecond range[10–14]. The possibility to manipulate these excitons via the twist angle between the two TMD layers[15–18] and the appearance of spin-valley and many-body physics[19–24] made TMD-based heterobilayers even more interesting in the emerging fields of both valleytronics and twistronics[1–3]. However, most studies focus on pure exciton physics and do not address the questions, if and how valley-polarized excitons in such heterobilayers can transfer their valley polarization to free charge carriers in either their conduction or valence bands, and if such a transfer mechanism can be controlled by parameters like the twist-angle or the position of the Fermi level. Answers to these questions are crucial for the realization of opto-valleytronic devices, in which the optically excited valley polarization may be extracted and measured by electrical means.

In this article, we report on an optical excitation mechanism that transfers the valley polarization from excitons in WSe_2 to free charge carriers in $MoSe_2$ via an interlayer charge transfer in twisted $WSe_2/MoSe_2$-heterobilayers. We show that this transfer of valley polarization significantly depends on both the twist angle and the position of the Fermi level. In devices with large twist angles (LTAs), the interlayer valley transfer becomes most efficient when crossing the band edges of both the $MoSe_2$ valence and conduction band. This behavior is explained by twist angle-dependent scattering mechanisms that involve the Q- and Γ-valleys, where the latter is probed by angle-resolved photoemission spectroscopy (ARPES). To measure both the valley polarization and the respective valley lifetimes, we employ an all-optical, time-resolved Kerr rotation (TRKR) measurement technique that has proven to be a powerful tool to investigate the valley dynamics[25–35]. In TRKR, circularly polarized laser pump pulses are typically used to resonantly excite valley-polarized excitons, while their temporal dynamics is being probed by linearly polarized laser probe pulses measuring the Kerr rotation angle. If the energy of the probe pulse is tuned to the trion (charged exciton) energy of the TMD material, TRKR is able to detect a valley polarization of free charge carriers in the corresponding TMD layer, as demonstrated in ref. [36] and discussed in the Supplementary Note 2. Therefore, for all measurements in this study, the pump and probe energies are the trion energies of the specified TMD unless stated otherwise.

We investigate five $WSe_2/MoSe_2$-heterobilayer devices (see schematic device layout in Fig. 1a and details on the device fabrication in the Method section) with varying twist angles, which were determined by polarization-dependent measurements of the second harmonic generation (see Supplementary Note 1 and [37]). The devices can be divided into two subgroups, which, as we will show, have substantially different valley dynamics: The first subgroup has a small twist angle (STA) towards a well-defined

[1]2nd Institute of Physics and JARA-FIT, RWTH Aachen University, 52074 Aachen, Germany. [2]AMO GmbH, Advanced Microelectronic Center Aachen (AMICA), 52074 Aachen, Germany. [3]Institut für Theoretische Physik, Universität Regensburg, D-93040 Regensburg, Germany. [4]Department of Applied Physics, Stanford University, 348 Via Pueblo Mall, Stanford, CA 94305, USA. [5]Peter Grünberg Institute (PGI-6), Forschungszentrum Jülich GmbH, 52428 Jülich, Germany. [6]Fakultät für Physik and Center for Nanointegration Duisburg-Essen (CENIDE), Universität Duisburg-Essen, D-47048 Duisburg, Germany. [7]Research Center for Functional Materials, National Institute for Materials Science, Tsukuba 305-0044, Japan. [8]International Center for Materials Nanoarchitectonics, National Institute for Materials Science, Tsukuba 305-0044, Japan. [9]Peter Grünberg Institute (PGI-9), Forschungszentrum Jülich, 52425 Jülich, Germany. [10]JARA-FIT Institute for Quantum Information, Forschungszentrum Jülich GmbH and RWTH Aachen University, 52074 Aachen, Germany. ✉email: volmer@physik.rwth-aachen.de

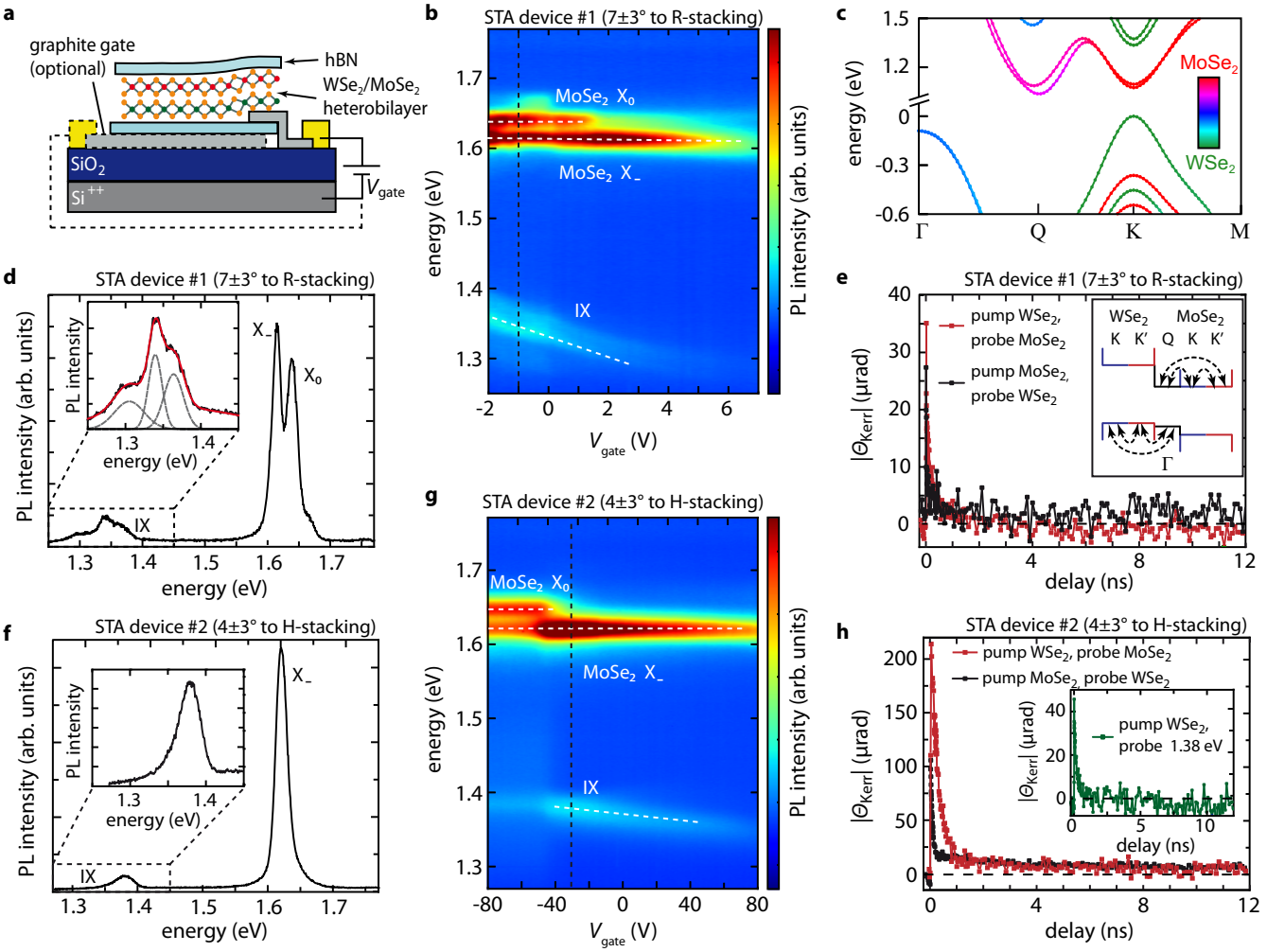

Fig. 1 Photoluminescence and time-resolved Kerr rotation measurements on $WSe_2/MoSe_2$ heterobilayers with small twist angles towards a crystallographic stacking order. a Schematic device structure of the heterobilayer devices. Only STA device #1 and LTA devices #1 and #3 have a graphite gate, whereas STA device #2 is gated via the Si^{++}/SiO_2 (285 nm) wafer. **c** Calculated band structure in case of the RhX-stacking (i.e., a twist angle of zero), in which the amount of hybridization is color-coded. The bands at the K-point only show negligible hybridization and a type-II band alignment. The bands at the Q- and Γ-valleys are strongly hybridized and, depending on parameters like stacking order or twist angle, shift in energy with respect to the band maxima at the K-point (see Supplementary Note 4). **b**, **g** Photoluminescence (PL) spectra as a function of gate voltage V_{gate} for two different devices plotted with a logarithmic color scale and (**d**, **f**) respective line-cuts plotted on a linear scale along the black dashed lines in (**b**) and (**g**) (white dashed lines are guides to the eye). The features with the highest PL intensities are the intralayer neutral exciton (X_0) and the trion (X_-) emission of $MoSe_2$. For STA device #1, the interlayer exciton (IX) emission consists of several sub-peaks (see fits in the inset of **d**), which can be attributed to transitions involving Q- and Γ-valleys. As these features are absent in STA device #2 (see inset in **f**), we assume that in STA device #2 both Q- and Γ-valleys are energetically further away from the K-valleys decreasing phonon-assisted scattering between the valleys (see schematic in the inset of **e**). This assumption is consistent to the TRKR data shown in (**e**, **h**). For STA device #1, we observe surprisingly short lifetimes of around 200 ps and extremely small amplitudes. Instead, Kerr rotation lifetimes and amplitudes of STA device #2 are one order of magnitude larger. All measurements were conducted at 10 K, pump and probe energies are the trion energies of the specified TMD unless stated otherwise.

crystallographic stacking order (an R-type stacking order for a twist angle of zero, an H-type stacking order for a twist angle of 60°[18,24,38,39]), while the second subgroup has a LTA with respect to these stacking orders.

RESULTS

Heterobilayers with small twist angles

We start our discussion with a $WSe_2/MoSe_2$ heterobilayer that has a STA of 7 ± 3° towards an R-type stacking order (STA device #1). A photoluminescence (PL) measurement as a function of the gate voltage V_{gate} is shown in Fig. 1b, whereas Fig. 1d depicts a line-cut along the black dashed line of Fig. 1b. The two features with the highest PL intensities are the intralayer neutral exciton (X_0) and trion (X_-) emission of $MoSe_2$. One observation that will get relevant as soon as we compare this device to ones that have larger twist angles is the absence of any intralayer PL emission from WSe_2. We note that even the PL emission from $MoSe_2$ is significantly reduced compared to the monolayer case, which can be attributed to an ultrafast charge transfer from intralayer into interlayer excitons[15,40–42]. In fact, a majority of the photo-excited electron-hole pairs must have been scattered into the interlayer exciton state (IX) to explain the appearance of its emission in Fig. 1b despite its very small oscillator strength[43,44]. The interlayer exciton appears between 1.3 and 1.4 eV and shows the expected gate-dependent energy shift due to its dipole moment[7,20] (dashed white lines in Fig. 1b are guides to the eye).

In this device, the interlayer exciton emission consists of several sub-peaks (see fits in the inset of Fig. 1d) which exact origins are still a debated topic[45]. Some studies argue that these sub-features can be related to transitions involving Q- and Γ-valleys[12,18,19,44,46,47]. If this is the case, the appearance of these sub-features would imply a strong hybridization between the two TMD layers. To address this, we refer to band structure calculations that predict that the bands at the K-point of the heterobilayer only show negligible signs of hybridization, i.e., that the conduction band minimum at the K-point of the heterobilayer mainly consists of $MoSe_2$ states, whereas the valence band maximum at the K-point mainly consists of WSe_2 states, leading to a type-II band alignment[44,46–48] (see Fig. 1c for the calculated band structure in case of the RhX-stacking). On the other hand, the bands at both the Q- and Γ-valleys are strongly hybridized and, depending on parameters like stacking order and twist angle, may shift in energy towards the band maxima at the K-point (see Supplementary Note 4 for more calculations). Interestingly, different studies significantly differ in the prediction of these energy shifts. Some of them claim a transition to an indirect semiconductor as either the Q-valley shifts below the K-point's conduction band minimum, or the Γ-valley shifts above the K-point's valence band maximum[44,46–49]. As we observe the sub-features in the interlayer exciton emission, we assume that both the Q- and Γ-valleys are energetically close enough to the K-valleys that phonon-assisted scattering can take place between these valleys (see schematic in the inset of Fig. 1e).

This finding is important for the interpretation of the TRKR data shown in Fig. 1e, where we plot the Kerr rotation amplitude Θ_{Kerr} vs the time delay between pump (circularly polarized) and probe (linearly polarized) pulses. Regardless where we set the pump and probe energies or which gate voltage we apply, we observe surprisingly short lifetimes of around 200 ps and small amplitudes of $\Theta_{Kerr} < 40$ µrad. The only Kerr rotation signal with a good enough signal-to-noise ratio to be analyzed was obtained by tuning the pump and probe energies to the trion energies of WSe_2 and $MoSe_2$ (see Fig. 1e). Instead, no signal was detected at the interlayer exciton energies (not shown). This is highly surprising in two ways: On the one hand, these values fall significantly short compared to lifetimes of up to nanoseconds and amplitudes of up to several hundreds of µrad that are typically observed in TRKR measurements on monolayer TMDs[25–34,36]. On the other hand, and even more surprising, is the fact that the lowest valley lifetimes of interlayer excitons measured by time- and helicity-resolved PL measurements in $WSe_2/MoSe_2$-heterobilayers are also in the nanosecond range[10–14]. Although we observe interlayer excitons in PL (see Fig. 1b), we conclude that TRKR is in all likelihood unable to directly detect the interlayer exciton valley polarization (see further discussion in Supplementary Note 3). Moreover, the short lifetimes in TRKR probed at the trion energies (Fig. 1e) imply that any valley polarization of free charge carriers relaxes quite fast in this heterobilayer. We attribute this to the aforementioned presence of the Γ- and Q-valleys, which provide additional scattering channels for a valley polarization as soon as these valleys are energetically in the phonon-assisted scattering range (see inset in Fig. 1e). This indicates the importance of these valleys in the understanding of the overall spin and valley dynamics of free charge carriers in heterobilayers that have STAs near to a crystallographic stacking order, which is in accordance with previous theoretical and experimental studies based on optical measurement techniques other than TRKR[4,40].

To support this notion, we studied another $WSe_2/MoSe_2$ heterobilayer (STA device #2) with a twist angle of $56 \pm 3°$, which is a STA of $4 \pm 3°$ to an H-type stacking order. This device also shows interlayer excitons in the gate-dependent PL map (see Fig. 1g), but without any well separated sub-peaks (see inset in Fig. 1f, which is a line-cut along the black dashed line in Fig. 1g). This may imply that the Q- and Γ-valleys are energetically further separated from the K-valleys and therefore no longer play a key role in the interlayer exciton emission. The less pronounced hybridization compared to STA device #1 might be due to the different stacking order (see also our calculations in Supplementary Note 4), an increased separation between the layers, or strain[50,51]. If we assume a larger energy separation between the K-valleys and the Q- or Γ-valleys, we expect a less pronounced scattering rate between these valleys. This is in complete accordance to the results of the TRKR measurements on this device, which yield Kerr rotation lifetimes and amplitudes which are one order of magnitude larger than the ones of STA device #1 (compare Fig. 1e, h). Setting the energies of the pump and probe laser pulses to the trion energies of the respective TMD layers, we now observe a fast decaying Kerr rotation signal of several hundreds of picoseconds and a second smaller signal with a decay in the nanosecond range. Interestingly, we even observe a small Kerr rotation signal when the probe pulse is set to the interlayer exciton energy (see the inset of Fig. 1h). However, it must be the topic of further studies to clarify, if this signal really originates from the interlayer exciton or is rather caused by a low-energy tail of a bright, intralayer exciton resonance (see, e.g., the discussions to Fig. 2b, c later on).

Heterobilayers with large twist angles

An even smaller impact of the Q- and Γ-valleys due to a larger energy separation to the K-valleys is expected for twist angles that are far away from a crystallographic stacking order (see calculations in Supplementary Note 4). Therefore, we now focus on a heterobilayer with a LTA of $23 \pm 3°$ (LTA device #1). The gate-dependent PL map of this device is shown in Fig. 2a and reveals a significantly different coupling between the two TMD layers. This is evident not only in the absence of an interlayer exciton emission[18], but also in the appearance of the intralayer exciton (X_0) and trion peaks (X_- and X'_-) of WSe_2[52–54], which were completely quenched in the previous two devices (compare Fig. 2a to Fig. 1b, g). It is important to note that many studies about $WSe_2/MoSe_2$-heterobilayers that are showing interlayer exciton emission show a much stronger quenching of WSe_2 intralayer excitons compared to the quenching of $MoSe_2$ intralayer excitons[7,11,13,17,23,47]. This implies the existence of fast, hybridization-induced scattering channels for photo-excited electron-hole pairs away from the K-valleys of WSe_2 in heterobilayers with STA (see Supplementary Note 4 for a more detailed discussion). Conversely, the appearance of the WSe_2 intralayer emission in LTA device #1 implies the suppression of these scattering channels for larger twist angles and therefore a significant decrease in the coupling strength between the TMD layers.

The conclusion of a decreased coupling is further supported by the TRKR measurements on LTA device #1 (Fig. 2b) that exhibit lifetimes and amplitudes that are much higher than those of the STA devices (compare Fig. 2b to Fig. 1e, h). In fact, amplitudes of hundreds of µrad and lifetimes in the nanosecond range are reminiscent to values measured on monolayer TMDs[25–34,36]. The energy scan in Fig. 2c, in which the pump pulse energy was fixed at the trion energy of WSe_2 and the probe pulse was tuned over the whole energy range of the PL measurements, only shows resonances at the bright intralayer exciton and trion energies. A small Kerr rotation signal at the interlayer exciton energy (between 1.3 and 1.4 eV in case of the STA devices), which is scaled-up by a factor of 100 in Fig. 2b for better visibility, is only due to the long tail of the bright exciton resonances in Fig. 2c.

Interestingly, two distinctly different TRKR signals can be revealed in the heterobilayer by tuning the Fermi level via a gate voltage and by varying the energies of both pump and probe pulses (see Fig. 2d–f for the respective amplitudes Θ_{Kerr} of the TRKR signals and the Supporting Information of ref. [36] for the used

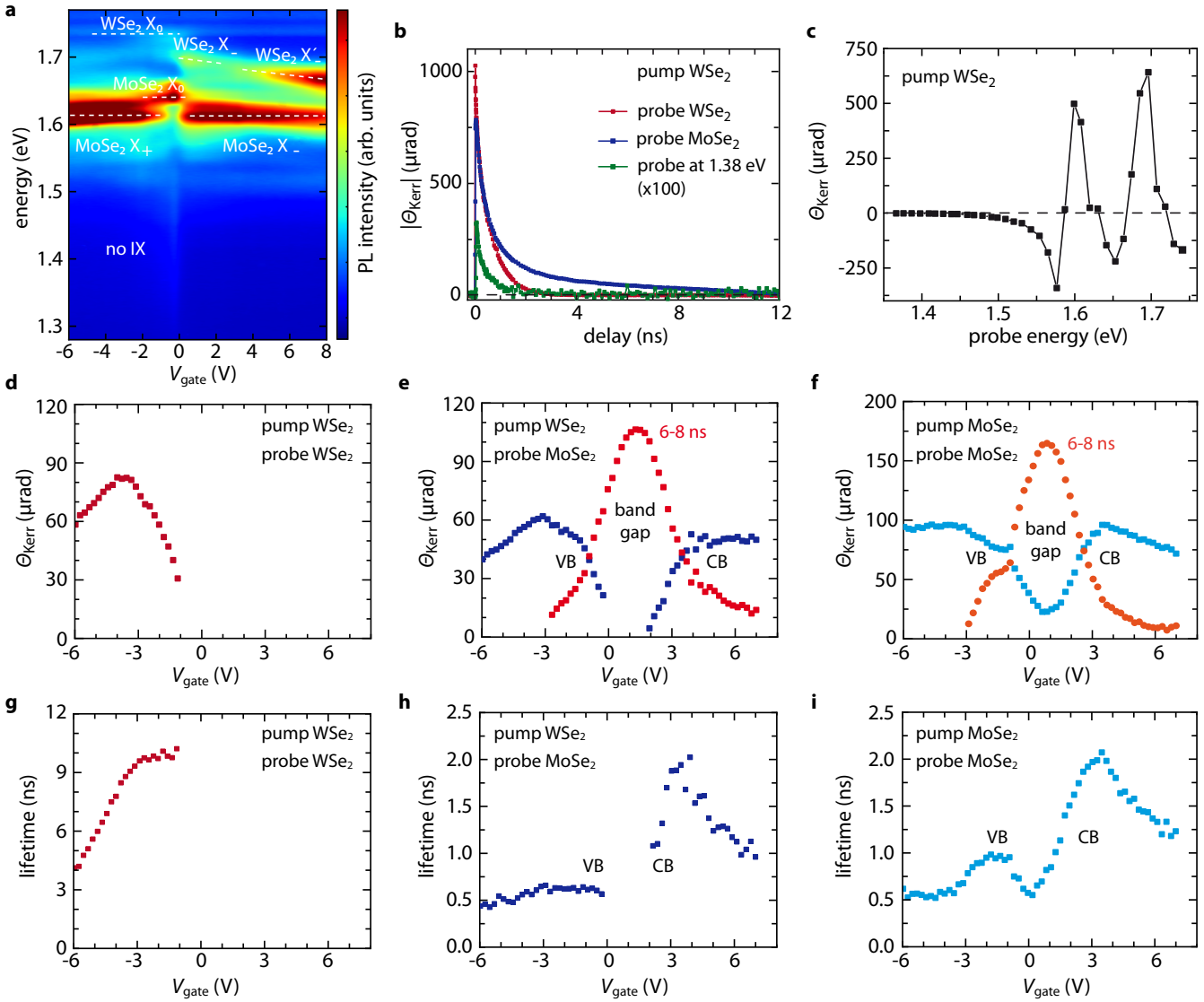

Fig. 2 Photoluminescence and time-resolved Kerr rotation measurements on a $WSe_2/MoSe_2$ heterobilayer with a large twist angle of 23 ± 3° (LTA device #1). a The gate-dependent PL spectra that are plotted on a logarithmic color scale show no interlayer exciton emission, but instead the intralayer exciton (X_0) and trion peaks (X_- and X'_-) of WSe_2. The latter were absent in Fig. 1b, g because of hybridization-induced scattering channels in devices with small twist angles. **b** Conversely, the appearance of the WSe_2 intralayer emission in LTA device #1 implies the suppression of these scattering channels, resulting in TRKR lifetimes and amplitudes that are much larger than the ones of the previous devices. **c** An energy scan, where the pump pulse energy is set to the trion energy of WSe_2 and the probe pulse energy is varied, only shows resonances at the bright intralayer exciton and trion energies. A Kerr rotation signal at the interlayer exciton energy, which is scaled-up by a factor of 100 in (**b**) for better visibility, is only due to the long tail of the bright exciton resonances. (**d–f**) Gate-dependent TRKR amplitudes and (**g–i**) lifetimes for different combinations of pump and probe energies, which reveal two different types of signals. The first signal (reddish colors) appears if the Fermi level lies in the band gap region of the probed TMD layer and can be linked to defect-bound exciton states. The second signal (blueish colors) appears as soon as the Fermi level is tuned either into the conduction (CB) or valence band (VB) of $MoSe_2$ (compare to the appearance of the trion features in (**a**)) and can be attributed to a valley polarization of free charge carriers (see explanation in the text). All measurements were conducted at 10 K, pump and probe energies are the trion energies of the specified TMD unless stated otherwise.

fitting procedure). The occurrence of these two signals depends on whether the Fermi level is tuned either in the band gap of the probed TMD layer (reddish colors in Fig. 2d–f) or in the valence or conduction band (blueish colors). For example, if we set the energies of both the pump and probe pulses to the trion energy of WSe_2 (Fig. 2d), a Kerr rotation signal with a lifetime between 4 and 10 ns (Fig. 2g) appears as soon as the trion emission of WSe_2 in Fig. 2a vanishes for gate voltages smaller than 0 V, i.e., as soon as we leave the conduction band and enter the band gap of WSe_2. If the probe pulse energy is instead tuned to the trion energy of $MoSe_2$ (see Fig. 2e, f, where we used different pump energies), a TRKR signal with similarly long lifetimes appears in the gate voltage range that also shows the appearance of the neutral exciton (X_0) emission of $MoSe_2$ in Fig. 2a, which in turn marks the gate range of the band gap in $MoSe_2$. Similar long-lived states within the gate voltage range, in which emission of neutral excitons predominates, have been reported previously in both $WSe_2/MoSe_2$ heterobilayers[55] and WSe_2 monolayer devices[36,56].

The corresponding amplitude of this long-lived signal is maximal within the band gap region and falls as soon as the Fermi level enters either the conduction band (VB) or valence band (VB) of $MoSe_2$, where the band edges are determined by the

appearance of the negatively or positively charged trion emission in Fig. 2a, respectively. Small shifts in the gate-dependent positions of the features in Fig. 2a compared to Fig. 2d–f are expected due to photo-induced gate screening effects that depend on both the energy and intensity of the used laser systems, which are different for TRKR and PL measurements (see ref. [57] and the Supporting Information of ref. [36]). As we discuss further below in more detail, the band gap related TRKR signal results from defect-bound exciton states within the band gap. Accordingly, the corresponding TRKR signal has a lifetime similar to the recombination time of these bound exciton states, which spans the nanosecond to microsecond range at cryogenic temperatures[58–60].

A distinctly different TRKR signal in the $WSe_2/MoSe_2$ heterobilayer appears when the Fermi level gets tuned into either the valence or the conduction band of $MoSe_2$ and when the probe energy is tuned to $MoSe_2$ (see blueish colors in Fig. 2e, f). The initial increase of the Kerr rotation amplitude indicates that this signal is linked to a valley-polarization of free charge carriers. Interestingly, such a gate-dependent TRKR signal is completely missing if both the pump and probe energies are set to the WSe_2 energy (Fig. 2d). Remarkably, this result is exactly opposite to what was found in the respective monolayer cases, as some of us demonstrated in ref. [36]. There, a valley polarization of free charge carriers could only be achieved in WSe_2, where the polarization mechanism was explained by an intervalley scattering channel via dark trion states, which are not available in $MoSe_2$ monolayers[52]. Comparing Fig. 2d, e instead reveals the existence of a mechanism that transfers the valley polarization from excitons in WSe_2 to free charge carriers in $MoSe_2$ via an interlayer charge transfer.

Deviation from the expected type-II band alignment

To explain this intriguing charge transfer process, we first discuss the PL data in Fig. 2a in more detail to determine the band structure of LTA device #1 and the gate-dependent position of the Fermi level. There is a striking gate-tunability of the WSe_2 trion emission, which shows a pronounced red-shift and a transition from the X_- to the X'_- trions, which is normally seen in monolayers of WSe_2[61,62], but to our knowledge has not yet been reported in such clarity in $WSe_2/MoSe_2$-heterobilayers. The exact origin of the X'_--feature is still under debate: Whereas in earlier publications it was attributed to the filling of the energetically higher, spin-split conduction band of WSe_2, more recent publications explain this feature with a coupling between plasmons and excitons or the creation of many-body exciton states[63–66]. Whatever its exact origin is, the appearance of this feature is only expected if the conduction band of WSe_2 at the K-point gets filled with electrons. However, this is unexpected in case of a type-II WSe_2 to $MoSe_2$ band alignment with well-separated conduction band minima of WSe_2 and $MoSe_2$ (see Fig. 1c)[44,46–48,67]. It was proposed that large displacement fields or high gate-induced charge carrier densities can reduce the energy separation between the conduction band minima of WSe_2 and $MoSe_2$ at the K-point, which eventually may even lead to a transition from a type-II to a type-I band alignment[9,68,69]. However, this explanation cannot be applied to LTA device #1 as the trion emission of both $MoSe_2$ and WSe_2 in Fig. 2a appear almost simultaneously at gate voltages that are only slightly larger than 0 V. Hence, it seems that the conduction band minima of $MoSe_2$ and WSe_2 are aligned close to each other, which allows the Fermi level E_F to almost simultaneously enter both conduction bands (see schematics in Fig. 3a, d, the blue lines in the figures represent spin-up and red lines represent spin-down bands, slightly opaque rectangles represent the filling of the respective bands with charge carriers). We propose that this unexpected band alignment might be caused by a combination of the LTA together with a slight *n*-doping of both the WSe_2 and $MoSe_2$ (note that in all PL maps, i.e., Figs. 1b, g, 2a, and 4a, the strongest emission of the neutral exciton is observed at gate voltages $V_{gate} < 0$ V, especially in Figs. 1g and 4a it is clear that the negatively charged trion emission prevails over the neutral exciton emission at $V_{gate} = 0$ V). The donor states may originate either from chalcogenide vacancies or substitutional dopants[70,71]. Before stacking the TMD layers into a heterostructure, the respective Fermi level in each TMD layer is therefore not in the middle of the band gap, but somewhere between the donor states and the conduction band minimum. Similar to conventional bulk semiconductors, we expect that the band alignment in the TMD heterostructure will be determined in first order approximation (i.e., ignoring any charge transfer processes) by the alignment of these two Fermi levels. Assuming similar donor binding energies (black solid lines below the conduction bands in Fig. 3a, d represent donor states) we therefore conclude that the conduction band minima of both TMD layers must be close to each other.

For the given band alignment we expect that for negative gate voltages the Fermi level first enters the valence band of $MoSe_2$, due to the smaller band gap of $MoSe_2$ compared to WSe_2 (see Fig. 3d). Ignoring any type of band renormalization that might be caused by photo-exited or gate-induced charge carriers[9,72,73], the valence band maximum of WSe_2 in Fig. 3d cannot be reached within a technically achievable gate voltage range. This is indeed in accordance to the PL data of Fig. 2a that shows the appearance of the positively charged trion (X_+) of $MoSe_2$ for $V_{gate} < -1$ V, but no clear tuning into the positively charged trion regime of WSe_2 (note that we have chosen a logarithmic color scale for all PL maps, the very small emission in the trion energy range of WSe_2 for $V_{gate} < 0$ V can be readily attributed to strain-induced band fluctuations at bubbles in the heterostructure[74,75]).

Whereas the PL measurements in Fig. 2a provide information about the respective band alignment at the K-valleys, we employ ARPES measurements to get further information about the relative position of the Γ-valley with respect to the K-valleys. Depending on stacking order, interlayer distance, or twist angle, theoretical studies come to different conclusions about whether the valence band maximum lies either at the Γ- or the K-valley[44,46–49]. Interestingly, even experimental ARPES studies come to different conclusions: Whereas one of the first reported measurements claims that the Γ-valley lies below the K-valley[76], a more recent measurement claims the opposite[77]. As we cannot conduct ARPES measurements on the devices with a top hexagonal boron nitride (hBN) layer (see Fig. 1a), we fabricated another heterobilayer (LTA device #2) with a twist angle comparable to LTA device #1. We used the same crystals and fabrication methods that were used for the other devices and placed a $MoSe_2/WSe_2$/graphite-stack directly onto an *n*-doped silicon wafer (i.e., with $MoSe_2$ on top, which therefore contributes most to the surface-sensitive ARPES measurements).

The ARPES measurements are shown in Fig. 3b, e for both s- and p-polarized light with a photon energy of 50 eV. The answer to the question in which valley the valence band maximum lies is made more difficult by the fact that the signal strength of an individual valley state depends on the polarization. Whereas the Γ-valley can be measured quite well with p-polarized light (Fig. 3b), the K-valleys are better visible with s-polarized light (Fig. 3e). Only considering linecuts that are normalized and averaged over a small wave-vector range at the K-, K′-, and Γ-points of the ARPES measurements with p-polarized light therefore may lead to the erroneous conclusion that the Γ-valley is slightly higher in energy than the K-valleys (see Fig. 3c). Instead, considering both the s- and p-polarized measurements and comparing linecuts that show the highest intensity for each individual valley demonstrates that the valence band maximum is rather located at the K-valleys (see Fig. 3f). However, Γ- and K-valleys are energetically close enough to each other that phonon-mediated scattering between these valleys is most likely more relevant than it already is in case of monolayer TMDs[27,40,78–82].

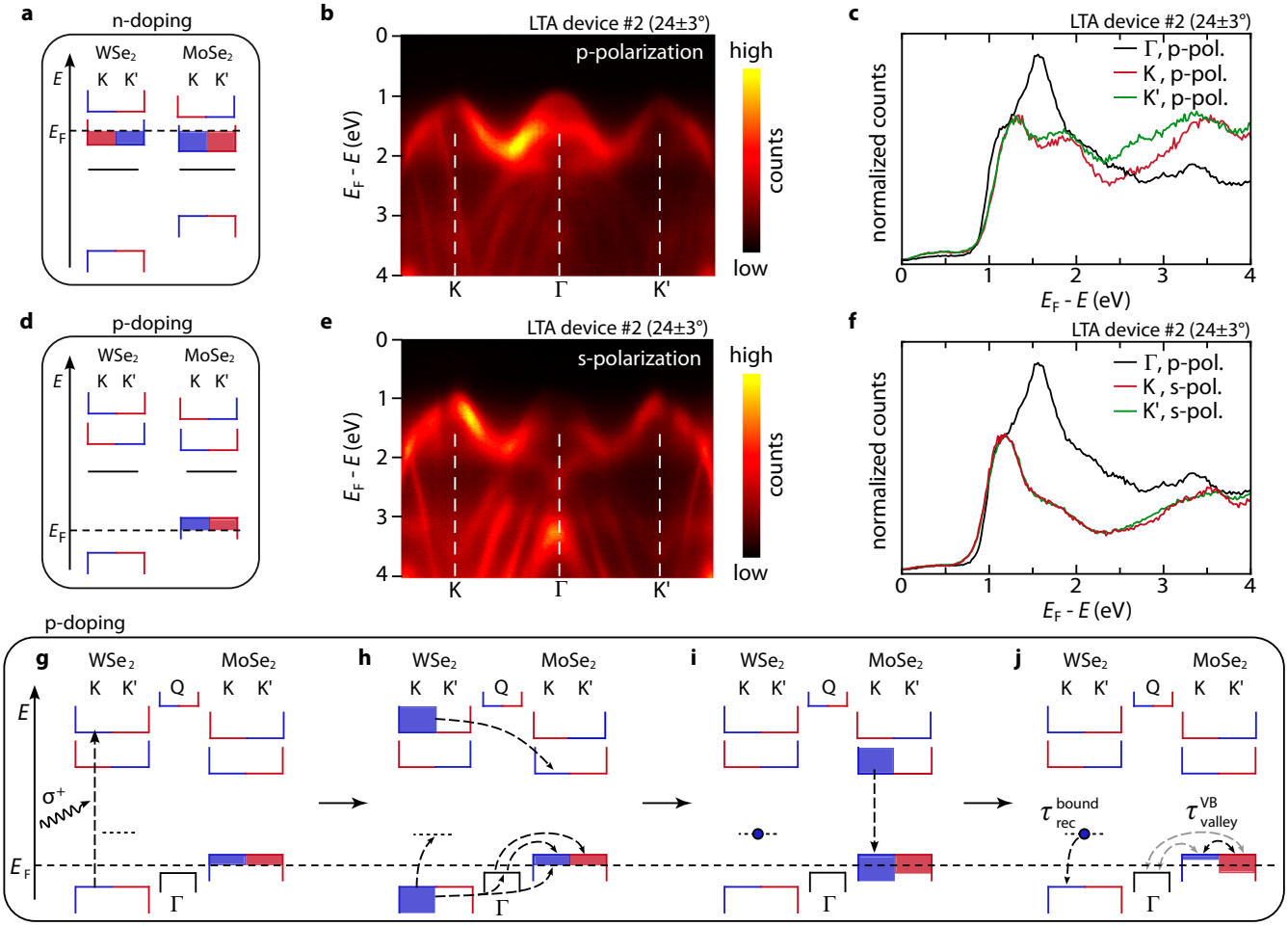

Fig. 3 Band structure at the K-, Q- and Γ-valleys for LTA devices and the resulting transfer mechanism of a valley polarization from excitons to free charge carriers. a, **d** Band structure of LTA device #1 at the K-points derived from the gate-dependence of the bright exciton emission in Fig. 2a. Blue and red colors represent spin-up and spin-down states, respectively. Sightly opaque rectangles represent the filling of the bands with charge carriers. **a** The fact that the negatively charged trion features of WSe_2 and $MoSe_2$ appear almost at the same gate voltage in Fig. 2a hints to an alignment of the respective conduction band minima to each other. This deviation from the expected type-II band alignment may be caused by a combination of the large twist angle together with a slight *n*-doping of both TMD layers (black solid lines below the conduction bands in (**a**, **d**) represent donor states). **d** For negative gate voltages, the smaller band gap of $MoSe_2$ prevents the Fermi level to enter the valence band of WSe_2 within the applicable gate voltage range, explaining the absence of the positively charged trion emission of WSe_2. **b**, **e** ARPES measurements of LTA device #2 for both s- and p-polarized light and (**c**, **f**) linecuts that are normalized and averaged over a small wave-vector range at the K-, K′-, and Γ-points demonstrate that in this device the Γ-valley is energetically close to the K-valleys. **g–j** Model that is based on the derived and measured band structure in (**a–f**) and that can explain both the energy and the gate dependence of the Kerr data in Fig. 2. See text for a detailed explanation.

Based on these ARPES results, we assume that in the other LTA devices the Γ-valley is also energetically lower than the K-valleys of $MoSe_2$, however energetically close enough such that the Γ-valley lies in between the K-valleys of WSe_2 and $MoSe_2$ (see schematic in Fig. 3g). It is also important that our DFT calculations show that the Γ-valley is spin-degenerate, whereas the Q-valley is showing a small spin-splitting (see Fig. 1c and Supplementary Note 4), which is consistent to previous studies[44,46,47,83].

Model of the interlayer transfer mechanism

With this knowledge, we now provide a model that explains the observed dependence of the valley polarization (Kerr rotation amplitude) in Fig. 2d–f on both the pump/probe energy and the gate. Figure 3g–j show the underlying dynamics for the case that the energy of the pump laser is set to WSe_2 and the Fermi level enters the valence band of $MoSe_2$, i.e., $-6\,V < V_{gate} < -1\,V$ in Fig. 2. Under such conditions, the right circularly polarized pump pulse will excite charge carriers from the upmost valence band of WSe_2 to its upper spin-split conduction band (see transition from Fig. 3g–h)[52]. It is likely that the predominant energy relaxation path for the photo-excited electrons involves an interlayer transfer from the upper spin-split conduction band of WSe_2 to the lower spin-split conduction band of $MoSe_2$, with the same spin-orientation and the same K-valley (see upper black dashed line in Fig. 3h). In contrast, the photo-excited holes can experience spin scattering caused by the spin-degenerate Γ-valley (see transition from Fig. 3h–i) leading to a population of the K′-valley's valence band with photo-exited holes.

The different interlayer spin/valley-scattering paths and rates of the photo-excited electrons and holes lead to a situation where eventually more photo-exited electrons than photo-excited holes are in the K-valley of $MoSe_2$, whereas the situation is reversed in the K′-valley (see Fig. 3i). During exciton recombination (see transition from Fig. 3i–j), photo-excited electrons also recombine with free holes in the K-valley, pushing the charge carrier density below the Fermi level (continuous dashed black line through Fig. 3g–j). As there are more photo-excited holes than electrons in the

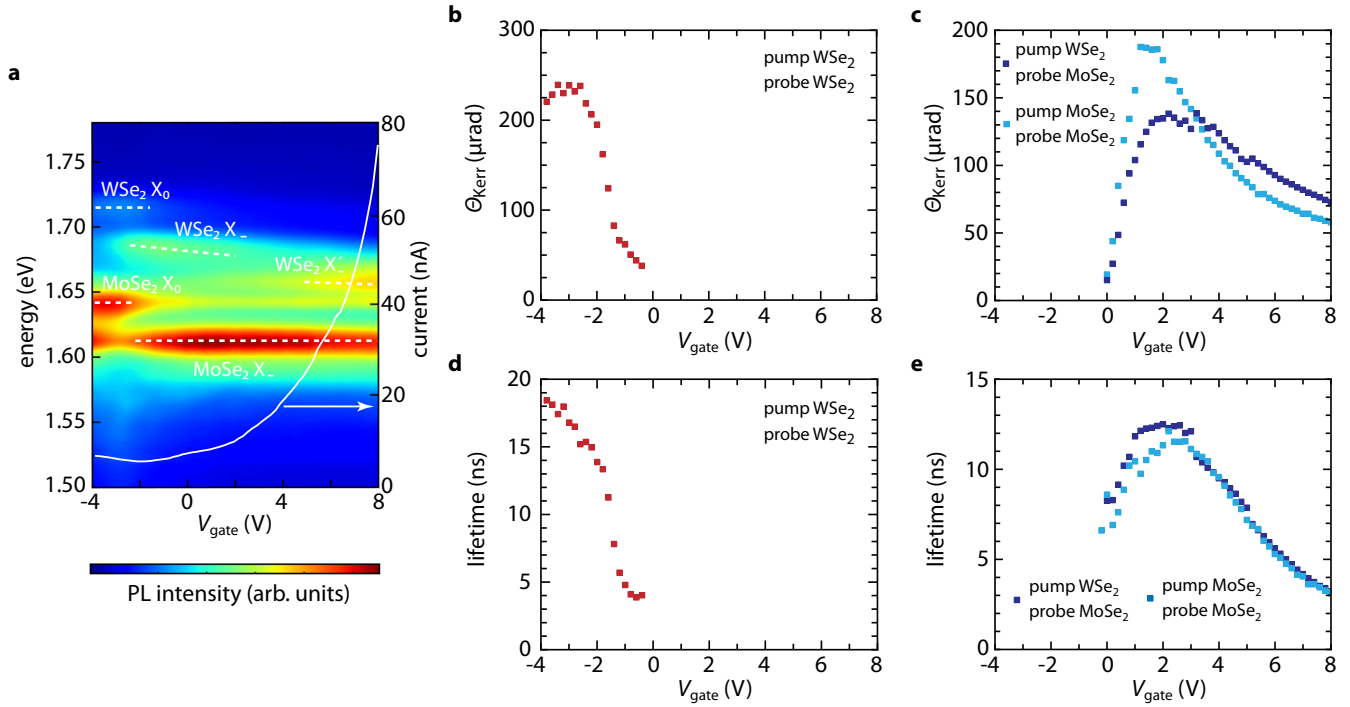

Fig. 4 Photoluminescence and time-resolved Kerr rotation measurements on a third $WSe_2/MoSe_2$ heterobilayer with large twist angle (LTA device #3). a The gate-dependent PL map of LTA device #3 that is plotted on a logarithmic color scale is also showing intralayer exciton emission of WSe_2, comparable to LTA device #1 in Fig. 2a. Because LTA device #3 was built with several graphite contacts, electrical transport measurements could be conducted on this device. The white line depicts the current at a bias voltage of 2 V. **b** The bound-exciton related Kerr rotation signal has the highest amplitude at the gate voltage range at which the neutral exciton emission in (**a**) indicates the position of the band gap. **c** The Kerr signal that can be attributed to a valley polarization of free charge carriers appears as soon as the current in (**a**) starts to rise at a gate voltage of around $V_{gate} = 0$ V. **d**, **e** Lifetimes of the signals in (**b**) and (**c**), respectively. All measurements were conducted at 10 K, pump and probe energies are the trion energies of the specified TMD.

K'-valley, it now shows a surplus of holes after the recombination process. Overall, this mechanism transfers the valley polarization from excitons to free charge carriers by a valley selective interlayer charge transfer. The resulting valley polarization then relaxes back into the equilibrium state with the genuine valley lifetime τ_{valley}^{VB} (see Fig. 3j).

The same interlayer transfer mechanism can be readily applied to the case in which the Fermi level is tuned into the conduction band of $MoSe_2$, resulting in a net valley polarization of free charge carriers in the conduction band. As the Q-valley plays a less significant role in the scattering process than the Γ-valley, we expect, however, that the respective valley lifetimes in the conduction band are longer than the ones in the valence band, which is indeed observed in our data (see Fig. 2h, i). Our model can also explain the great similarity between Fig. 2e, h on the one hand and Fig. 2f, i on the other hand, i.e., between setting the pump energy either to WSe_2 or $MoSe_2$. Creating electron-hole pairs directly in the K-valley of $MoSe_2$ would lead to the exact same condition that is depicted in Fig. 3i, if we assume that the photo-excited holes will be subjected to scattering via the Γ-valley. Despite the energy separation of the Γ-valley from the K-valleys of $MoSe_2$, this scattering is very likely to occur during the short timescale of the pump pulse because of photo-induced band gap renormalization effects and the amount of available phonons that are created by the scattering of photo-excited charge carriers into lower-energy states[72,73,84,85].

Finally, the long-lived Kerr rotation signal that is present when the Fermi level lies within the band gap of one of the two TMD layers (reddish data points in Fig. 2d–f) can be explained by the mechanism that was discussed in ref. [36] and can be easily incorporated into our current model: A part of the photo-excited electron-hole pairs scatter into defect-bound exciton states (see Fig. 3h), which can have quite long recombination times τ_{rec}^{bound} from the nanosecond up to the microsecond range[58–60] and also may create a valley polarization of resident charge carriers during their recombination process (Fig. 3j). As this polarization process is directly connected to the lifetime of the bound excitons, i.e., the polarization occurs during the full exciton recombination time, it does not allow the direct probing of the respective valley lifetimes (see rate equation model in the Supplemental Material of ref. [36] for a more detailed discussion).

We note that we simplified our model in Fig. 3g–j in the sense that we did only consider the most important scattering and recombination channels. However, the consideration of, e.g., additional spin-flip scattering processes or non-radiative recombination processes does not change the overall result, as long as the photo-excited electrons and holes undergo differently strong valley scattering processes. Here a simplified explanation for this necessary condition: If the photo-excited holes recombine with the photo-excited electrons in the same valley (either the valley in which they were created or in which both were scattered into) the system will end up in its initial state, which means that no net valley polarization of free charge carriers can be induced. Instead, with different scattering rates for electrons and holes, there will be an imbalance of photo-excited charge carriers in the conduction and valence bands of a specific valley and, therefore, their recombination necessitates the involvement of resident (free) charge carriers, which get polarized during the recombination process.

Counter-play of two different scattering channels

Finally, we explore another device with large twist angle (LTA device #3), which additionally allows for charge transport

measurements as it was built with multiple graphite contacts. The gate-dependent PL map of this device (Fig. 4a) is quite comparable to the one of LTA device #1 in Fig. 2a, especially with respect to the appearance of the exciton emission of WSe_2. When tuning both pump and probe energies to WSe_2 we again observe the long-lived Kerr rotation signal (Fig. 4b, d) that is related to the bound exciton states and that has its largest amplitude at the gate voltage range where the neutral exciton of WSe_2 is most pronounced in Fig. 4a.

The white solid line in Fig. 4a depicts the source-drain current measured at a bias voltage of 2 V and shows that the current starts to rise at a gate voltage of around $V_{gate} = 0$ V. It is exactly at this gate voltage at which the TRKR signal that can be attributed to the valley polarization of free charge carriers appears when the probe energy is tuned to $MoSe_2$ (see Fig. 4c). Its amplitude first increases almost linearly with the gate voltage (the more free charge carriers are induced by the gate, the more can be polarized), before it eventually decreases again for larger gate voltages, i.e., larger electron densities, which is in complete accordance to LTA device #1. The respective valley lifetimes are shown in Fig. 4e, whereas Fig. 4d shows the lifetime of the bound-exciton driven signal. As it was the case for LTA device #1 (see Fig. 2h, i), the valley lifetime of the free charge carriers (Fig. 4e) first increases for small carrier densities, then exhibit a maximum at intermediate densities, before it eventually decreases towards higher densities. We attribute this overall trend to an interplay of two different scattering channels that have opposite dependencies with respect to the Fermi level. Pushing the Fermi level further into the conduction band reduces the scattering via mid-gap or tail states. However, at the same time, wave-vector dependent electron-phonon and spin-orbit scattering mechanisms get stronger[36,81,86,87].

We note that when probing at the $MoSe_2$ energy, LTA device #3 does not exhibit any long-lived, bound-exciton related Kerr rotation signal when the Fermi level is tuned into the band gap. This indicates a low defect density in the $MoSe_2$ layer. At the same time, we observe much longer valley lifetimes of free charge carriers compared to LTA device #1 (up to 12 ns instead of 2 ns). Combining these two observations supports the notion that mid-gap or tail states limit the genuine valley lifetime for small charge carrier densities.

DISCUSSION

In summary, we have demonstrated that the twist angle has a significant impact on the dynamics of valley-polarized free charge carriers in $WSe_2/MoSe_2$ heterobilayers. For small twist angles near a crystallographic stacking order (an R-type stacking order for a twist angle of zero, an H-type stacking order for a twist angle of 60°), scattering via Q- and Γ-valleys highly diminishes the valley polarization of free charge carriers, despite the simultaneous occurrence of interlayer excitons with their presumably long recombination and polarization times. For twist angles that lie between these stacking orders, we observe a substantial increase in both the magnitude and the lifetime of the valley polarization, hinting to a significant reduction in the scattering via the Q- and Γ-valleys. Gate-dependent measurements of these latter devices enable us to disentangle two different Kerr signals, one that is related to defect-bound states within the band gap region, and one that represents the actual valley-polarization of free charge carriers within either valence or conduction band. Interestingly, for these devices we also observe a deviation from the widely assumed type-II band alignment that we contribute to an alignment of the respective conduction bands by donor states. This observation could open the possibility of tailoring the band alignment in these heterobilayer devices, and thus the valley and spin dynamics, by using differently doped TMD layers. Most importantly, the unexpected band structure alignment in these devices enables an interlayer transfer of photo-induced, valley-polarized excitons from the WSe_2 layer into a pronounced valley polarization of free charge carriers in the $MoSe_2$ layer. This transfer is most efficient at the onsets of either valence or conduction band, demonstrating the possibility of extracting and utilizing this valley polarization by electrical means.

METHODS

Device fabrication

The $WSe_2/MoSe_2$-heterobilayer devices are fabricated from exfoliated flakes with a dry-transfer method, protected by hBN from both sides and contacted via graphite electrodes (see schematic in Fig. 1a; detailed information about device fabrication can be found in refs. [36,88]). For STA device #1 and LTA devices #1 and #3 we furthermore incorporated a graphite gate, whereas for STA device #2 we use the Si^{++}/SiO_2 (285 nm) wafer for gating. An exception from this general fabrication procedure is LTA device #2 that is used for the ARPES measurements and therefore cannot be protected by hBN. For this device we directly placed a $MoSe_2/WSe_2$/graphite-stack onto an n-doped silicon wafer.

Measurements

Detailed technical information about the TRKR and PL measurement techniques and the used fitting procedures can be found in the Supporting Information sections of refs. [27,34,36]. We note that it is important to account for photo-induced screening effects of the gate electric field[57] to unveil the true lifetimes and amplitudes of the Kerr signal that can be attributed to free charge carriers. In the Supporting Information of ref. [36] we show how the standard optical measurement techniques can be modified to account for the photo-induced gate screening and we demonstrate that disregarding this procedure can lead to erroneous conclusions drawn from gate-dependent measurements.

Time-resolved Kerr rotation

Two mode-locked Ti:sapphire lasers are used to independently tune the energies of both pump and probe pulses. An electronic delay between both pulses covers the full laser repetition interval of 12.5 ns. The pulse widths are on the order of 3 ps. The laser beams are focused onto the device by a 15 mm focal length aspheric lens (numerical aperture of 0.66 NA). Typical spot diameters are 6−8 µm measured as a full width at half maximum (FWHM) value. The laser power was around 500 µW for both pump and probe beams.

Photoluminescence

A microscope objective lens (numerical aperture of 0.5 NA) is used for the photoluminescence measurement. The resulting spot size is around 1–2 µm FWHM. A continuous wave laser with an energy of 2.33 eV and a power between 10 and 50 µW is used for these measurements.

Angle-resolved photoemission spectroscopy

The ARPES measurements have been performed at the NanoESCA beamline of Elettra, the Italian synchrotron radiation facility, using a FOCUS NanoESCA photoemission electron microscope (PEEM) in the k-space mapping mode operation[89]. The PEEM is operating at a background pressure $p < 5 \times 10^{-11}$ mbar and the photoelectron signal is collected from a spot size of about 5−10 µm. Before the experiment the sample was outgassed in UHV at $T = 180$ °C for 60 min. The measurements were conducted with a photon energy of 50 eV and an overall energy resolution of 50 meV using p- and s-polarized synchrotron radiation, while keeping the sample at 90 K.

DATA AVAILABILITY

All data are available from the corresponding author on request.

Received: 25 January 2023; Accepted: 10 August 2023;
Published online: 22 August 2023

REFERENCES

1. Ciarrocchi, A., Tagarelli, F., Avsar, A. & Kis, A. Excitonic devices with van der Waals heterostructures: valleytronics meets twistronics. *Nat. Rev. Mater.* **7**, 449–464 (2022).
2. Schaibley, J. R. et al. Valleytronics in 2D materials. *Nat. Rev. Mater.* **1**, 16055 (2016).
3. Mueller, T. & Malic, E. Exciton physics and device application of two-dimensional transition metal dichalcogenide semiconductors. *npj 2D Mater. Appl.* **2**, 29 (2018).
4. Jiang, Y., Chen, S., Zheng, W., Zheng, B. & Pan, A. Interlayer exciton formation, relaxation, and transport in TMD van der Waals heterostructures. *Light Sci. Appl.* **10**, 72 (2021).
5. Liu, Y. et al. Valleytronics in transition metal dichalcogenides materials. *Nano Res.* **12**, 2695–2711 (2019).
6. Jauregui, L. A. et al. Electrical control of interlayer exciton dynamics in atomically thin heterostructures. *Science* **366**, 870–875 (2019).
7. Ciarrocchi, A. et al. Polarization switching and electrical control of interlayer excitons in two-dimensional van der Waals heterostructures. *Nat. Photonics* **13**, 131–136 (2019).
8. Kiemle, J. et al. Control of the orbital character of indirect excitons in MoS_2/WS_2 heterobilayers. *Phys. Rev. B* **101**, 121404 (2020).
9. Meng, Y. et al. Electrical switching between exciton dissociation to exciton funneling in $MoSe_2$/WS_2 heterostructure. *Nat. Commun.* **11**, 2640 (2020).
10. Rivera, P. et al. Valley-polarized exciton dynamics in a 2D semiconductor heterostructure. *Science* **351**, 688–691 (2016).
11. Rivera, P. et al. Observation of long-lived interlayer excitons in monolayer $MoSe_2$-WSe_2 heterostructures. *Nat. Commun.* **6**, 6242 (2015).
12. Miller, B. et al. Long-lived direct and indirect interlayer Excitons in van der Waals Heterostructures. *Nano Lett.* **17**, 5229–5237 (2017).
13. Jiang, C. et al. Microsecond dark-exciton valley polarization memory in two-dimensional heterostructures. *Nat. Commun.* **9**, 753 (2018).
14. Nagler, P. et al. Giant magnetic splitting inducing near-unity valley polarization in van der Waals heterostructures. *Nat. Commun.* **8**, 1551 (2017).
15. Zimmermann, J. E. et al. Ultrafast charge-transfer dynamics in twisted MoS_2/WSe_2 heterostructures. *ACS Nano* **15**, 14725–14731 (2021).
16. Yuan, L. et al. Twist-angle-dependent interlayer exciton diffusion in WS_2-WSe_2 heterobilayers. *Nat. Mater.* **19**, 617–623 (2020).
17. Choi, J. et al. Twist angle-dependent interlayer Exciton lifetimes in van der Waals Heterostructures. *Phys. Rev. Lett.* **126**, 047401 (2021).
18. Nayak, P. K. et al. Probing evolution of twist-angle-dependent interlayer Excitons in $MoSe_2$/WSe_2 van der Waals Heterostructures. *ACS Nano* **11**, 4041–4050 (2017).
19. Sigl, L. et al. Signatures of a degenerate many-body state of interlayer excitons in a van der Waals heterostack. *Phys. Rev. Res.* **2**, 042044 (2020).
20. Li, W., Lu, X., Dubey, S., Devenica, L. & Srivastava, A. Dipolar interactions between localized interlayer excitons in van der Waals heterostructures. *Nat. Mater.* **19**, 624–629 (2020).
21. Jin, C. et al. Identification of spin, valley and moiré quasi-angular momentum of interlayer excitons. *Nat. Phys.* **15**, 1140–1144 (2019).
22. Shimazaki, Y. et al. Strongly correlated electrons and hybrid excitons in a moiré heterostructure. *Nature* **580**, 472–477 (2020).
23. Kremser, M. et al. Discrete interactions between a few interlayer excitons trapped at a $MoSe_2$-WSe_2 heterointerface. *npj 2D Mater. Appl.* **4**, 8 (2020).
24. Woźniak, T., Faria Junior, P. E., Seifert, G., Chaves, A. & Kunstmann, J. Exciton *g* factors of van der Waals heterostructures from first-principles calculations. *Phys. Rev. B* **101**, 235408 (2020).
25. Kumar, A. et al. Spin/valley coupled dynamics of electrons and holes at the MoS_2-$MoSe_2$ interface. *Nano Lett.* **21**, 7123–7130 (2021).
26. Kravtsov, V. et al. Spin-valley dynamics in alloy-based transition metal dichalcogenide heterobilayers. *2D Mater.* **8**, 025011 (2021).
27. Ersfeld, M. et al. Spin states protected from intrinsic electron-phonon coupling reaching 100 ns lifetime at room temperature in $MoSe_2$. *Nano Lett.* **19**, 4083–4090 (2019).
28. Song, X., Xie, S., Kang, K., Park, J. & Sih, V. Long-lived hole spin/valley polarization probed by Kerr Rotation in Monolayer WSe_2. *Nano Lett.* **16**, 5010–5014 (2016).
29. Yang, L. et al. Long-lived nanosecond spin relaxation and spin coherence of electrons in monolayer MoS_2 and WS_2. *Nat. Phys.* **11**, 830–834 (2015).
30. Kempf, M., Schubert, A., Schwartz, R. & Korn, T. Two-color Kerr microscopy of two-dimensional materials with sub-picosecond time resolution. *Rev. Sci. Instrum.* **92**, 113904 (2021).
31. McCormick, E. J. et al. Imaging spin dynamics in monolayer WS_2 by time-resolved Kerr rotation microscopy. *2D Mater.* **5**, 011010 (2017).
32. Zhu, C. R. et al. Exciton valley dynamics probed by Kerr rotation in WSe_2 monolayers. *Phys. Rev. B* **90**, 161302 (2014).
33. Plechinger, G. et al. Trion fine structure and coupled spin-valley dynamics in monolayer tungsten disulfide. *Nat. Commun.* **7**, 12715 (2016).
34. Volmer, F. et al. Intervalley dark trion states with spin lifetimes of 150 ns in WSe_2. *Phys. Rev. B* **95**, 235408 (2017).
35. Raiber, S. et al. Ultrafast pseudospin quantum beats in multilayer WSe_2 and $MoSe_2$. *Nat. Commun.* **13**, 4997 (2022).
36. Ersfeld, M. et al. Unveiling valley lifetimes of free charge carriers in monolayer WSe_2. *Nano Lett.* **20**, 3147–3154 (2020).
37. Hsu, W. T. et al. Second harmonic generation from artificially stacked transition metal dichalcogenide twisted bilayers. *ACS Nano* **8**, 2951–2958 (2014).
38. Rosenberger, M. R. et al. Twist angle-dependent atomic reconstruction and Moiré patterns in transition metal Dichalcogenide Heterostructures. *ACS Nano* **14**, 4550–4558 (2020).
39. Faria Junior, P. E. & Fabian, J. Signatures of electric field and layer separation effects on the spin-valley physics of $MoSe_2$/WSe_2 Heterobilayers: from energy bands to dipolar Excitons. *Nanomaterlals* **13**, 1187 (2023).
40. Jin, C. et al. Ultrafast dynamics in van der Waals heterostructures. *Nat. Nanotechnol.* **13**, 994–1003 (2018).
41. Hong, X. et al. Ultrafast charge transfer in atomically thin MoS_2/WS_2 heterostructures. *Nat. Nanotechnol.* **9**, 682–686 (2014).
42. Ji, Z. et al. Robust stacking-independent ultrafast charge transfer in MoS_2/WS_2 bilayers. *ACS Nano* **11**, 12020–12026 (2017).
43. Ovesen, S. et al. Interlayer exciton dynamics in van der Waals heterostructures. *Commun. Phys.* **2**, 23 (2019).
44. Gillen, R. & Maultzsch, J. Interlayer excitons in $MoSe_2$/WSe_2 heterostructures from first principles. *Phys. Rev. B* **97**, 165306 (2018).
45. Deilmann, T., Rohlfing, M. & Wurstbauer, U. Light-matter interaction in van der Waals hetero-structures. *J. Phys. Condens. Matter* **32**, 333002 (2020).
46. Okada, M. et al. Direct and indirect interlayer Excitons in a van der Waals heterostructure of hBN/WS_2/MoS_2/hBN. *ACS Nano* **12**, 2498–2505 (2018).
47. Hanbicki, A. T. et al. Double indirect interlayer Exciton in a $MoSe_2$/WSe_2 van der Waals Heterostructure. *ACS Nano* **12**, 4719–4726 (2018).
48. Zheng, Q. et al. Phonon-coupled ultrafast interlayer charge oscillation at van der Waals heterostructure interfaces. *Phys. Rev. B* **97**, 205417 (2018).
49. Hagel, J., Brem, S., Linderälv, C., Erhart, P. & Malic, E. Exciton landscape in van der Waals heterostructures. *Phys. Rev. Res.* **3**, 043217 (2021).
50. Zollner, K., Faria Junior, P. E. & Fabian, J. Strain-tunable orbital, spin-orbit, and optical properties of monolayer transition-metal dichalcogenides. *Phys. Rev. B* **100**, 195126 (2019).
51. Kunstmann, J. et al. Momentum-space indirect interlayer excitons in transition-metal dichalcogenide van der Waals heterostructures. *Nat. Phys.* **14**, 801–805 (2018).
52. Wang, G. et al. Colloquium: Excitons in atomically thin transition metal dichalcogenides. *Rev. Mod. Phys.* **90**, 021001 (2018).
53. Ye, Z. et al. Efficient generation of neutral and charged biexcitons in encapsulated WSe_2 monolayers. *Nat. Commun.* **9**, 3718 (2018).
54. Borghardt, S. et al. Radially polarized light beams from spin-forbidden dark excitons and trions in monolayer WSe_2. *Opt. Mater. Express* **10**, 1273–1285 (2020).
55. Jin, C. et al. Imaging of pure spin-valley diffusion current in WS_2-WSe_2 heterostructures. *Science* **360**, 893–896 (2018).
56. Li, J. et al. Valley relaxation of resident electrons and holes in a monolayer semiconductor: dependence on carrier density and the role of substrate-induced disorder. *Phys. Rev. Mater.***5**, 044001 (2021).
57. Volmer, F. et al. How photoinduced gate screening and leakage currents dynamically change the fermi level in 2D mater. *Phys. Status Solidi RRL* **14**, 2000298 (2020).
58. Goodman, A. J., Willard, A. P. & Tisdale, W. A. Exciton trapping is responsible for the long apparent lifetime in acid-treated MoS_2. *Phys. Rev. B* **96**, 121404 (2017).
59. Moody, G. et al. Microsecond valley lifetime of defect-bound Excitons in monolayer WSe_2. *Phys. Rev. Lett.* **121**, 057403 (2018).
60. Rivera, P. et al. Intrinsic donor-bound excitons in ultraclean monolayer semiconductors. *Nat. Commun.* **12**, 871 (2021).
61. Jones, A. M. et al. Optical generation of excitonic valley coherence in monolayer WSe_2. *Nat. Nanotechnol.* **8**, 634–638 (2013).
62. Wang, Z., Zhao, L., Mak, K. F. & Shan, J. Probing the spin-polarized electronic band structure in monolayer transition metal dichalcogenides by optical spectroscopy. *Nano Lett.* **17**, 740–746 (2017).
63. Wang, Z., Mak, K. F. & Shan, J. Strongly interaction-enhanced valley magnetic response in monolayer WSe_2. *Phys. Rev. Lett.* **120**, 066402 (2018).
64. Van Tuan, D., Scharf, B., Žutić, I. & Dery, H. Marrying Excitons and plasmons in monolayer transition-metal dichalcogenides. *Phys. Rev. X* **7**, 041040 (2017).

65. Van Tuan, D. et al. Probing many-body interactions in monolayer transition-metal dichalcogenides. *Phys. Rev. B* **99**, 085301 (2019).
66. Van Tuan, D., Shi, S.-F., Xu, X., Crooker, S. A. & Dery, H. Six-body and eight-body Exciton states in monolayer WSe_2. *Phys. Rev. Lett.* **129**, 076801 (2022).
67. Ponomarev, E., Ubrig, N., Gutiérrez-Lezama, I., Berger, H. & Morpurgo, A. F. Semiconducting van der Waals interfaces as artificial semiconductors. *Nano Lett.* **18**, 5146–5152 (2018).
68. Zhang, F., Li, W. & Dai, X. Modulation of electronic structures of $MoSe_2/WSe_2$ van der Waals heterostructure by external electric field. *Solid State Commun.* **266**, 11–15 (2017).
69. Huang, D. & Kaxiras, E. Electric field tuning of band offsets in transition metal dichalcogenides. *Phys. Rev. B* **94**, 241303 (2016).
70. Younas, R., Zhou, G. & Hinkle, C. L. A perspective on the doping of transition metal dichalcogenides for ultra-scaled transistors: challenges and opportunities. *Appl. Phys. Lett.* **122**, 160504 (2023).
71. Loh, L., Zhang, Z., Bosman, M. & Eda, G. Substitutional doping in 2D transition metal dichalcogenides. *Nano Res.* **14**, 1668 (2021).
72. Chernikov, A., Ruppert, C., Hill, H. M., Rigosi, A. F. & Heinz, T. F. Population inversion and giant bandgap renormalization in atomically thin WS_2 layers. *Nat. Photonics* **9**, 466–470 (2015).
73. Cunningham, P. D., Hanbicki, A. T., McCreary, K. M. & Jonker, B. T. Photoinduced Bandgap renormalization and Exciton binding energy reduction in WS_2. *ACS Nano* **11**, 12601–12608 (2017).
74. Shin, B. G. et al. Indirect Bandgap Puddles in Monolayer MoS_2 by Substrate-Induced Local Strain. *Adv. Mater.* **28**, 9378–9384 (2016).
75. Peng, Z., Chen, X., Fan, Y., Srolovitz, D. J. & Lei, D. Strain engineering of 2D semiconductors and graphene: from strain fields to band-structure tuning and photonic applications. *Light Sci. Appl.* **9**, 190 (2020).
76. Wilson, N. R. et al. Determination of band offsets, hybridization, and exciton binding in 2D semiconductor heterostructures. *Sci. Adv.* **3**, 1601832 (2017).
77. Khalil, L. et al. Hybridization and localized flat band in the $WSe_2/MoSe_2$ heterobilayer. *Nanotechnology* **34**, 045702 (2022).
78. Christiansen, D. et al. Phonon sidebands in monolayer transition metal dichalcogenides. *Phys. Rev. Lett.* **119**, 187402 (2017).
79. Raja, A. et al. Enhancement of Exciton-phonon scattering from monolayer to bilayer WS_2. *Nano Lett.* **18**, 6135–6143 (2018).
80. Liu, F., Li, Q. & Zhu, X.-Y. Direct determination of momentum-resolved electron transfer in the photoexcited van der Waals heterobilayer WS_2/MoS_2. *Phys. Rev. B* **101**, 201405 (2020).
81. Molina-Sánchez, A., Sangalli, D., Wirtz, L. & Marini, A. Ab Initio calculations of ultrashort carrier dynamics in two-dimensional materials: valley depolarization in single-layer WSe_2. *Nano Lett.* **17**, 4549 (2017).
82. Wang, Z. et al. Phonon-mediated interlayer charge separation and recombination in a $MoSe_2/WSe_2$ heterostructure. *Nano Lett.* **21**, 2165–2173 (2021).
83. Torun, E., Miranda, H. P. C., Molina-Sánchez, A. & Wirtz, L. Interlayer and intralayer excitons in MoS_2/WS_2 and $MoSe_2/WSe_2$ heterobilayers. *Phys. Rev. B* **97**, 245427 (2018).
84. Ruppert, C., Chernikov, A., Hill, H. M., Rigosi, A. F. & Heinz, T. F. The role of electronic and phononic excitation in the optical response of monolayer WS_2 after ultrafast excitation. *Nano Lett.* **17**, 644–651 (2017).
85. Katoch, J. et al. Giant spin-splitting and gap renormalization driven by trions in single-layer WS_2/h-BN heterostructures. *Nat. Phys.* **14**, 355–359 (2018).
86. Ochoa, H. & Roldán, R. Spin-orbit-mediated spin relaxation in monolayer MoS_2. *Phys. Rev. B* **87**, 245421 (2013).
87. Gunst, T., Markussen, T., Stokbro, K. & Brandbyge, M. First-principles method for electron-phonon coupling and electron mobility: applications to two-dimensional materials. *Phys. Rev. B* **93**, 035414 (2016).
88. Bisswanger, T. et al. CVD Bilayer Graphene Spin Valves with 26 μm Spin Diffusion Length at Room Temperature. *Nano Lett.* **22**, 4949–4955 (2022).
89. Schneider, C. M. et al. Expanding the view into complex material systems: from micro-ARPES to nanoscale HAXPES. *J. Electron Spectrosc. Relat. Phenom.* **185**, 330–339 (2012).
90. Albrecht, W., Moers, J. & Hermanns, B. HNF-Helmholtz Nano Facility. *J. Large Scale Res. Facil.* **3**, 112 (2017).

ACKNOWLEDGEMENTS

The authors thank Riccardo Reho, Pedro Miguel MC de Melo, Zeila Zanolli, and Matthieu Verstraete for helpful discussions. This project has received funding from the European Union's Horizon 2020 research and innovation program under grant agreement No 881603, by the Deutsche Forschungsgemeinschaft (DFG, German Research Foundation) under Germany's Excellence Strategy - Cluster of Excellence Matter and Light for Quantum Computing (ML4Q) EXC 2004/1 - 390534769, and by the Helmholtz Nanoelectronic Facility (HNF) at the Forschungszentrum Jülich[90]. P.E.F.J. and J.F. acknowledge the financial support of the Deutsche Forschungsgemeinschaft (DFG, German Research Foundation) SFB 1277 (Project-ID 314695032, projects B07 and B11), SPP 2244 (Project No. 443416183), and of the European Union Horizon 2020 Research and Innovation Program under Contract No. 881603 (Graphene Flagship). L.W. acknowledges support by the Alexander von Humboldt foundation. K.W. and T.T. acknowledge support from JSPS KAKENHI (Grant Numbers 19H05790, 20H00354 and 21H05233).

AUTHOR CONTRIBUTIONS

B.B., C.S. and F.V. conceived and supervised the project. M.E. performed the TRKR, PL, and electrical measurements with the support of F.V., L.R. and S.D. M.E. and F.V. analyzed the data from the TRKR, PL, and electrical measurements. P.E.F.J. and J.F. performed the first-principles calculations. L.W. performed and analyzed the SHG. F.V., M.E. and B.B. derived the model of the interlayer transfer mechanism. L.R., S.D. and B.P. designed and fabricated the devices. B.P., L.P., I.C., V.F. and C.M.S. performed, analyzed, and supervised the ARPES measurements. K.W. and T.T. synthesized the hBN crystals. F.V. and B.B. wrote the paper with contributions from all authors.

FUNDING

Open Access funding enabled and organized by Projekt DEAL.

COMPETING INTERESTS

The authors declare no competing interests.

ADDITIONAL INFORMATION

Supplementary information The online version contains supplementary material available at https://doi.org/10.1038/s41699-023-00420-1.

Correspondence and requests for materials should be addressed to Frank Volmer.

Reprints and permission information is available at http://www.nature.com/reprints

Publisher's note Springer Nature remains neutral with regard to jurisdictional claims in published maps and institutional affiliations.